

Generalized focusing of time-lapse changes with applications to direct current and time-domain induced polarization inversions

Gianluca Fiandaca,¹ Joseph Doetsch,^{1,2} Giulio Vignoli³ and Esben Auken¹

¹Department of Geoscience, Aarhus University, Aarhus, Denmark. E-mail: gianluca.fiandaca@geo.au.dk

²SCCER-SoE, Department of Earth Sciences, ETH Zurich, Zurich, Switzerland

³GEUS—Geological Survey of Denmark and Greenland, Aarhus, Denmark

Accepted 2015 August 18. Received 2015 July 7; in original form 2015 January 20

SUMMARY

Often in geophysical monitoring experiments time-lapse inversion models vary too smoothly with time, owing to the strong imprint of regularization. Several methods have been proposed for focusing the spatiotemporal changes of the model parameters. In this study, we present two generalizations of the minimum support norm, which favour compact time-lapse changes and can be adapted to the specific problem requirements. Inversion results from synthetic direct current resistivity models that mimic developing plumes show that the focusing scheme significantly improves size, shape and magnitude estimates of the time-lapse changes. Inversions of the synthetic data also illustrate that the focused inversion gives robust results and that the focusing settings are easily chosen. Inversions of full-decay time-domain induced polarization (IP) field data from a CO₂ monitoring injection experiment show that the focusing scheme performs well for field data and inversions for all four Cole–Cole polarization parameters. Our tests show that the generalized minimum support norms react in an intuitive and predictable way to the norm settings, implying that they can be used in time-lapse experiments for obtaining reliable and robust results.

Key words: Time-series analysis; Inverse theory; Electrical properties; Hydrogeophysics.

1 INTRODUCTION

Monitoring of subsurface changes by time-lapse inversion of geophysical data has been of increasing interest in recent years. In particular, direct current (DC) resistivity monitoring has become a common method in near-surface applications, due to acquisition automation options and the resolution capability at the relevant scale. Examples of DC resistivity monitoring comprise saline tracer injections (e.g. Slater *et al.* 2000; Doetsch *et al.* 2012), seasonal moisture variations (e.g. Binley *et al.* 2002), groundwater recharge (e.g. Descloitres *et al.* 2008), infiltration processes (e.g. French & Binley 2004), watershed characterization (e.g. Miller *et al.* 2008), permafrost studies (e.g. Hauck 2002) and thermal tracer test monitoring (Hermans *et al.* 2015). Recently, induced polarization (IP) data have been used in monitoring studies: in frequency domain for contamination monitoring (Chambers *et al.* 2004) and in bioremediation (Williams *et al.* 2009; Flores Orozco *et al.* 2011); in time domain, for biostimulation monitoring (Johnson *et al.* 2010), for mapping CO₂ transport (Doetsch *et al.* 2015a) and permafrost seasonal variations (Doetsch *et al.* 2015b). A detailed review of resistivity monitoring for hydrological applications can be found in Singha *et al.* (2014).

Usually time-lapse inversion of geophysical data is more sophisticated than the simple differentiation of models from separate

inversions. In particular, systematic measurement errors that are constant over time are attenuated by cancellation techniques, and model regularization is typically applied also with respect to temporal changes. Examples of time-lapse cancellation techniques are: (i) the ratio inversion, where the ratio of initial and subsequent data sets is inverted (Daily *et al.* 1992); (ii) the cascaded inversion, in which the initial data set is used for building the reference model that constrains the inversions of the subsequent data sets (Oldenborger *et al.* 2007; Miller *et al.* 2008); (iii) the difference inversion, in which the initial data set is used for building the reference model and for correcting the forward modeling inaccuracy (LaBrecque & Yang 2001). More recently, simultaneous inversion of two or more time steps has been also introduced in geophysical applications (Kim *et al.* 2009; Hayley *et al.* 2011; Karaoulis *et al.* 2011a,b; Kim *et al.* 2013), following the developments carried out in the biomedical field (Brooks *et al.* 1999).

Kim *et al.* (2009) inverted several data sets simultaneously and in their approach the 2-D/3-D resistivity structure can change continuously during data acquisition. Therefore, it is not required that the data acquisition at each time step is faster than the subsurface temporal changes. Another simple and robust approach to overcome the problem of a finite acquisition time for a complete data set and thus data available at different times is to interpolate all ERT data to common time stamps using spline interpolation (Coscia *et al.* 2012;

Doetsch *et al.* 2012) or geostatistical interpolation such as kriging (Auken *et al.* 2014a). Hayley *et al.* (2011) introduced two different approaches, namely the temporally constrained time-lapse inversion and the simultaneous time-lapse inversion. The two methods differ on the model regularization, but a single optimization procedure is used for inverting both data sets at once. Kim *et al.* (2013) introduced an approach in which several time-lapse data sets can be inverted in a unique inversion process and L1/L2 norms, which penalize either the absolute value or the squared value of the variations, can be used in the spatial and temporal directions. Furthermore, extra cross-time and resolution reweighting are introduced to avoid models that vary too smoothly with time and to reduce artefact contamination of the less resolved parameters. Karaoulis *et al.* (2011a, b) describe the so-called active time constrained (ATC) approach for focusing the spatiotemporal changes of the model parameters, where several time-lapse resistivity data sets can be inverted at once. The ACT approach tunes the time regularization depending on the degree of spatial changes occurring among different time steps for producing anomalies that are more compact. Consequently, this method requires a two-steps inversion approach, in which the data are first inverted in a more standard way, for tuning subsequently the spatiotemporal regularization. Another way of obtaining compact changes in time-lapse inversion is to use model norms that favour compactness directly, instead of adding extra reweighting terms in the linear algebra, as the cross-time and resolution matrices of Kim *et al.* (2013) or the ACT reweighting of Karaoulis *et al.* (2011a,b). In particular, the minimum support norm (Last & Kubik 1983; Portniaquine & Zhdanov 1999) provides the model with the minimum area of the changes in the parameter distribution. Ajo-Franklin *et al.* (2007) use the minimum support norm for focusing changes in differential traveltimes tomography. Rosas Carbajal *et al.* (2012) compare different norms, among which the minimum support one, for focusing time-lapse changes in radio and audio magnetotelluric inversions. Kim & Cho (2011) apply the minimum support norm to resistivity time-lapse inversion, while Hermans *et al.* (2014) use the minimum gradient support (which minimize the area where strong model parameter variations and discontinuity occur, Portniaquine & Zhdanov 1999) in time-lapse cross-hole resistivity monitoring.

In all these time-lapse applications of the minimum support norm, as well as in other applications of the minimum support (e.g. Last & Kubik 1983; Zhdanov & Tolstaya 2004; Minsley *et al.* 2007), different approaches are given for tuning the minimum support settings (a detailed discussion of these different approaches is given in the minimum support paragraphs of this study), but no examples are given of the effects of the tuning on the focusing results.

In this study, we focus our attention on both the effectiveness and the tuning of the minimum support norm, and we define two new generalized minimum support functionals that can be adjusted for time-lapse inversion with three settings: (i) the threshold defining the “transition” between changed and non-changed parameters, (ii) the maximum relative variation, and (iii) the sharpness of the transition. The transition threshold is a re-interpretation of the tuning setting of the classic minimum support functional, while the maximum relative variation and the transition sharpness (this latter defined symmetrically or asymmetrically around the transition threshold in the two generalizations, respectively) represent two new tuning settings. The introduction of these two new settings in the generalized minimum support functionals implies more degrees of freedom in the setting tuning, which in turn may simply add complexity and be counterproductive. On the contrary, studying the effects of these settings on the functionals and the inversion results

of 2-D DC synthetic models mimicking a developing plume, we show that it is possible to give an intuitive meaning to the functional settings and to define a strategy to choose the settings for optimal results.

This strategy and the performance of the proposed minimum support functional are further verified in a 2-D field application for monitoring of CO₂ injection in a shallow aquifer (Auken *et al.* 2014b; Doetsch *et al.* 2015a). The field example contains both DC and time-domain IP data, and all the DC and full-decay IP data are inverted in a single inversion process in terms of Cole–Cole parameters (Cole & Cole 1941; Pelton *et al.* 1978) following Fiandaca *et al.* (2013).

2 INVERSION SETUP

The time-lapse inversion scheme adopted in this study follows a sequential approach in which an initial data set is selected for computing a reference model $\mathbf{m}_{\text{reference}}$ and the subsequent data sets are inverted by constraining the model vector \mathbf{m} against the reference model $\mathbf{m}_{\text{reference}}$. Furthermore, roughness constraints are applied on the distance $\delta\mathbf{m}$ between the model vector \mathbf{m} and the reference model vector $\mathbf{m}_{\text{reference}}$ and the data misfit is corrected following the difference inversion approach (LaBrecque & Yang 2001). Consequently, the objective function Φ minimized in our time-lapse inversion scheme is composed by three terms:

$$\Phi = \Phi_d(\delta\mathbf{d}) + \Phi_{\text{TL}}(\delta\mathbf{m}) + \Phi_R(\delta\mathbf{r}) \quad (1)$$

where:

(1) Φ_d , Φ_{TL} and Φ_R represent the measures (i.e. the squared norms) of the data, model and roughness vectors, respectively; consequently, Φ_{TL} and Φ_R represent the regularization of the inversion, split in two terms: the time-lapse measure Φ_{TL} that constrains the distance between \mathbf{m} and $\mathbf{m}_{\text{reference}}$ and roughness measure Φ_R that favours smooth solutions.

(2) $\delta\mathbf{d} = (\mathbf{d} - \mathbf{d}_{\text{obs}}) - (\mathbf{d}_{\text{reference}} - \mathbf{d}_{\text{obs reference}})$ represents the difference between the forward response \mathbf{d} and the observed data \mathbf{d}_{obs} , corrected by the difference correction introduced by LaBrecque & Yang (2001) (where $\mathbf{d}_{\text{obs reference}}$ and $\mathbf{d}_{\text{reference}}$ represent the reference observed data and the forward response of the reference inversion model, respectively).

(3) $\delta\mathbf{r} = -\mathbf{R}(\delta\mathbf{m})$ is the roughness on $\delta\mathbf{m}$, computed through the roughness matrix \mathbf{R} .

The time-lapse inversion is performed iteratively, by following the established practice of linearized approximation of the non-linear forward mapping of the model to the data space, by the first term of the Taylor expansion (Menke 1989). Norms different from the L2 are implemented following the iteratively reweighted least-squares (IRLS) approach (Farquharson & Oldenburg 1998). The $(n + 1)$ th update of the model vector \mathbf{m} is obtained by:

$$\mathbf{m}_{(n+1)} = \mathbf{m}_{(n)} + \left[\mathbf{G}'_{(n)T} \mathbf{C}'_{(n)}{}^{-1} \mathbf{G}'_{(n)} + \lambda_{(n)} \mathbf{I} \right]^{-1} \cdot \left[\mathbf{G}'_{(n)T} \mathbf{C}'_{(n)}{}^{-1} \delta\mathbf{d}'_{(n)} \right] \quad (2)$$

where the parameter $\lambda_{(n)}$ is the iteratively updated (Auken *et al.* 2014a) damping parameter (Marquart 1963), and the Jacobian $\mathbf{G}'_{(n)}$, the data vector update $\delta\mathbf{d}'_{(n)}$ and the inverse of the covariance matrix $\mathbf{C}'_{(n)}{}^{-1}$ incorporate both the prior/time-lapse and the roughness

constraints and are defined as:

$$\mathbf{G}'_{(n)} = \begin{bmatrix} \mathbf{G}_{(n)} \\ \mathbf{I} \\ \mathbf{R} \end{bmatrix} \quad (3)$$

$$\delta \mathbf{d}'_{(n)} = \begin{bmatrix} \delta \mathbf{d}_{(n)} \\ \delta \mathbf{m}_{(n)} \\ \delta \mathbf{r}_{(n)} \end{bmatrix} \quad (4)$$

$$\mathbf{C}'_{(n)} = \begin{bmatrix} \mathbf{C}_{\text{obs}}^{-1} & 0 & 0 \\ 0 & \mathbf{W}'_{\text{TL}(n)} \mathbf{C}_{\text{TL}}^{-1} \mathbf{W}'_{\text{TL}(n)} & 0 \\ 0 & 0 & \mathbf{W}'_{R(n)} \mathbf{C}_R^{-1} \mathbf{W}'_{R(n)} \end{bmatrix} \quad (5)$$

In eq. (3), $\mathbf{G}_{(n)}$ represents the Jacobian of the forward mapping; \mathbf{I} is the identity matrix; \mathbf{R} is the roughness matrix.

In eq. (5), the covariance matrix \mathbf{C}' is defined in terms of the covariance on the observed data \mathbf{C}_{obs} , the time-lapse covariance on the reference information \mathbf{C}_{TL} and the covariance on the roughness constraints \mathbf{C}_R . The elements of \mathbf{C}_{TL} and \mathbf{C}_R control the strength of the model constraints, while the elements of \mathbf{C}_{obs} reflect the noise content of the data. All three matrices are diagonal, thus implying that no correlation is considered between data errors. In eq. (5) the matrices $\mathbf{W}'_{\text{TL}(n)}$ and $\mathbf{W}'_{R(n)}$ represent the (optional) re-weighting of the covariance matrices used to implement norms different from the L2. For a given model vector \mathbf{x} (equal to either $\delta \mathbf{m}$ or $\delta \mathbf{r}$) and a given measure functional $\Phi(\mathbf{x}) = \sum_{i=1}^{\text{size}(\mathbf{x})} \varphi(x_i)$, the matrices \mathbf{W}'_{η} (where $\eta = \text{TL}$ or $\eta = R$) are linked to the measure Φ and the covariance matrices \mathbf{C}_{η} following Farquharson & Oldenburg (1998):

$$W'_{\eta,i} = \sqrt{\frac{C_{\eta,i}}{2x_i}} \varphi'(x_i); \quad (6)$$

In this respect, the focusing implementation presented in this study differs from the one described by Vignoli *et al.* (2015), because in Vignoli *et al.* (2015) the Fréchet derivative of \mathbf{W}'_{η} were disregarded in the minimization of the object function.

The stopping criterion of the iterative procedure in eq. (2) is implemented on the total misfit χ , defined as:

$$\begin{aligned} \chi &= \left(\frac{\Phi_d(\delta \mathbf{d}) + \Phi_{\text{TL}}(\delta \mathbf{m}) + \Phi_R(\delta \mathbf{r})}{N_d + N_{\text{TL}} + N_R} \right)^{\frac{1}{2}} \\ &= \left(\frac{N_d \chi_d^2 + N_{\text{TL}} \chi_{\text{TL}}^2 + N_R \chi_R^2}{N_d + N_{\text{TL}} + N_R} \right)^{\frac{1}{2}} \end{aligned} \quad (7)$$

in which:

(1) N_d, N_{TL}, N_R represent the number of data points, the number of time-lapse constraints and the number of roughness constraints.

(2) $\chi_d = \left(\frac{\delta \mathbf{d}^T \mathbf{C}_{\text{obs}}^{-1} \delta \mathbf{d}}{N_d} \right)^{\frac{1}{2}}$ represents the data misfit.

(3) $\chi_{\text{TL}} = \left(\frac{\delta \mathbf{m}^T \mathbf{W}'_{\text{TL}} \mathbf{C}_{\text{TL}}^{-1} \mathbf{W}'_{\text{TL}} \delta \mathbf{m}}{N_{\text{TL}}} \right)^{\frac{1}{2}}$ represents the time-lapse model penalty.

(4) $\chi_R = \left(\frac{\delta \mathbf{r}^T \mathbf{W}'_R \mathbf{C}_R^{-1} \mathbf{W}'_R \delta \mathbf{r}}{N_R} \right)^{\frac{1}{2}}$ represents the roughness model penalty.

The matrices \mathbf{W}'_{η} (where $\eta = \text{TL}$ or $\eta = R$) are linked to the measure Φ and the covariance matrices \mathbf{C}_{η} as:

$$W_{\eta,i} = \sqrt{\frac{C_{\eta,i}}{x_i^2}} \varphi(x_i) \quad (8)$$

The inversion is stopped when the variation of the total misfit between two consecutive iterations is smaller than 1 per cent. Finally, the Jacobian $\mathbf{G}_{(n)}$ and the forward mapping $\mathbf{d}_{(n)}$ of eqs (2) and (3) are computed for 2-D DC and DC-IP data following Fiandaca *et al.* (2013), and the inversions are carried out in logarithmic data and model spaces.

3 CLASSIC AND GENERALIZED MINIMUM SUPPORT

3.1 Methodology

The classic minimum support functional is defined as (Last & Kubik 1983; Portniquaine & Zhdanov 1999):

$$\Phi_{\text{MS}}(\mathbf{x}) = \sum_{i=1}^{\text{size}(\mathbf{x})} \varphi_{\text{MS}}(x_i) = \sum_{i=1}^{\text{size}(\mathbf{x})} \frac{x_i^2}{x_i^2 + \varepsilon^2} \quad (9)$$

The role of ε in eq. (9) can be understood better considering the limit cases of $x_i \ll \varepsilon$ and $x_i \gg \varepsilon$: $\frac{x_i^2}{x_i^2 + \varepsilon^2}$ tends to 1 when $x_i \gg \varepsilon$, while $\frac{x_i^2}{x_i^2 + \varepsilon^2}$ tends to 0 when $x_i \ll \varepsilon$. In the limit of $\varepsilon \rightarrow 0$ the minimum support functional ‘counts’ the number of vector elements different from zero, while for $\varepsilon \rightarrow \infty$ the measure of the vector is always zero. Consequently, the effectiveness of the minimum support in focusing anomalies depends strongly on the ε -value. Several procedures have been proposed in the literature for selecting the ε -value, for instance:

(1) Last & Kubik (1983) suggest for ε^2 ‘a sufficiently small value’ and claim that ‘a choice of ε^2 of the order of the machine precision ($\approx 10^{-11}$ in our case) gives good results’.

(2) Zhdanov & Tolstaya (2004) plot $\Phi_{\text{MS}}(\mathbf{x}_{L_2}, \varepsilon)$ versus ε and ‘chose ε to be in the vicinity of the maximum convex curvature point’, where \mathbf{x}_{L_2} is the L2 solution of the inverse problem.

(3) Zhdanov *et al.* (2006) and Ajo-Franklin *et al.* (2007) ‘fix ε at a reasonable value determined by experience’ that is typically between 10^{-3} and 10^{-7} .

(4) Rosas Carbajal *et al.* (2012) ‘have found that taking $\varepsilon = \sum_{i=1}^N \frac{|x_i|}{N}$ leads to satisfactory solutions for all cases considered’.

(5) Kim & Cho (2011) claim that ‘it is quite difficult to determine a globally optimal value’ for ε and suggest to compute it as $\varepsilon_i = \varepsilon_{\text{min}} + \frac{\varepsilon_{\text{max}} - \varepsilon_{\text{min}}}{\delta p_{\text{max}} - \delta p_{\text{min}}} (\delta p_{\text{max}} - \delta p_i)$, where δp_i , in our notation, correspond to $\frac{m_i - m_{\text{reference}_i}}{m_{\text{reference}_i}}$.

(6) Vignoli *et al.* (2012) suggest that, in order to prevent singularities, ε^2 should satisfy the inequalities $\frac{\varepsilon^2}{x_i^2} \geq \text{eps}$ (where eps is the machine floating-point relative accuracy) and, consequently, ε^2 can be effectively chosen equal to $\text{eps} \cdot \max(\mathbf{x})^2$.

All these approaches for the choice of ε are quite different one from the other. Furthermore, in none of these studies inversion results are shown when varying the ε -value (to our knowledge, only in Blaschek *et al.* (2008) results with varying ε are shown, but this study is not discussed here because it uses the minimum gradient support functional instead of the minimum support for focusing inversion results). In our opinion, a better understanding of how to select ε in the specific case of time-lapse inversions can be achieved when looking at the $\varphi_{\text{MS}}(x)$ function in logarithmic x scale, as shown in Fig. 1. In fact, ε represents the transition point for the minimum support measure (with $\varphi_{\text{MS}}(\varepsilon) = 0.5$), and a change in ε simply translates the function along the (logarithmic) x -axis.

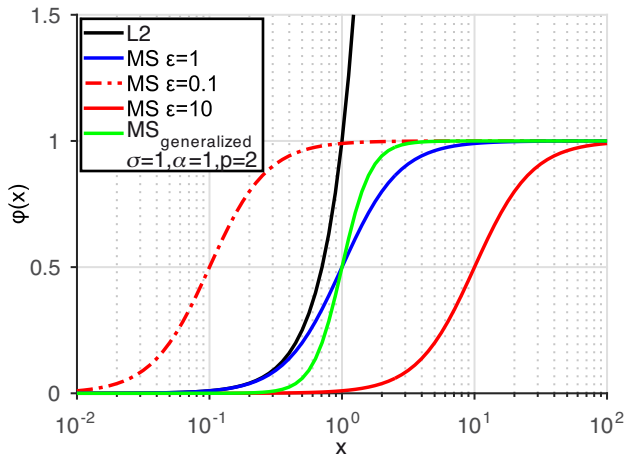


Figure 1. Comparison of classic minimum support (eq. 9) and generalized minimum support (eqs 10a and 10b) with varying norm settings.

A ‘transition’ concept can be introduced for resistivity time-lapse experiments as well. In fact, in such experiments it is often possible to predict the order of magnitude of the expected parameter variations: for example, the resistivity variation is due to the change in water saturation and/or in water conductivity and Archie’s law (Archie 1942) can be used for forecasting the parameter changes. But if the prediction of the parameter variation is not trivial, for instance when reactive processes occur in concomitance with flow and transport processes, the classic L2 inversion can be used for estimating the order of magnitude of the parameter variation. Consequently, the threshold (i.e. ε) can be selected in function of the expected variation, and a minimum support functional can be used to ‘measure’ the time-lapse changes. In this way, the parameters that vary more than the threshold represent the time-lapse changes, while the parameters that change less than the threshold are only weakly penalized.

The minimum support has been implemented in this study following these concepts, with the following generalization:

$$\Phi_{\text{MS}_{\text{generalized}}}(\mathbf{x}) = \sum_{i=1}^{\text{size}(\mathbf{x})} \varphi_{\text{MS}_{\text{generalized}}}(x_i) \quad (10a)$$

$$\varphi_{\text{MS}_{\text{generalized}}}(x_i) = \alpha^{-1} \frac{(x_i^2/\sigma_i^2)^p}{(x_i^2/\sigma_i^2)^p + 1} = \alpha^{-1} \frac{(x_i^2/C_{\eta_i,i})^p}{(x_i^2/C_{\eta_i,i})^p + 1} \quad (10b)$$

where ε has been substituted with the σ_i symbol (linked to the variance of eq. (5), that is, $\sigma_i^2 = C_{\eta_i,i}$, with $\eta = \text{TL}$ or $\eta = R$) and the settings α and p have been introduced. In the case of $\alpha = 1$, $p = 1$ and a logarithmic model space, eqs (10a) and (10b) reduces to eq. (9), with $\sigma_i = \varepsilon$.

The symbol σ_i represents the threshold value, expressed as a fraction of reference parameter values (typically a fixed percentage). When inverting in logarithmic model space, or against a homogeneous model, the σ_i values are therefore constant for all the elements of the $\mathbf{x} = \delta\mathbf{m}$ vector. But σ_i is parameter-dependent when inverting in linear model space against a generic reference model. In this case, eqs (9) and (10a,b) differ significantly, even when using $\alpha = p = 1$.

The symbol p in eq. (10b) controls the sharpness of the transition: the higher the p -value, the sharper the transition. With $p = 2$ one decade around σ_i is needed to reach 99 per cent of the asymptotic values (i.e. 0 or 1), compared to the two decades needed with $p = 1$ (see Fig. 1, blue and green lines comparison).

Finally, the symbol α in eq. (10b) controls the relative weight between data and model measures in the objective function and together with σ_i determines the model compactness. In fact, α is linked to the number of transitions $N_{\text{Transitions}} := \sum_{i=1}^{\text{size}(\mathbf{x})} \frac{(x_i^2/C_{\eta_i,i})^p}{(x_i^2/C_{\eta_i,i})^p + 1}$ ‘counted’ by the minimum support functional, as evident when putting together this definition of $N_{\text{Transitions}}$ and the definition of χ_{TL} (see eq. 7):

$$\chi_{\text{TL}}^2 = \frac{\Phi_{\text{MS}}(\delta\mathbf{m})}{N_{\text{TL}}} = \alpha^{-1} \frac{N_{\text{Transitions}}}{N_{\text{TL}}} \quad (11)$$

Please note that with the aforementioned definition, $N_{\text{Transitions}}$ is not an integer number.

If in a time-lapse experiment it is possible to estimate the number of expected transitions $N_{\text{Transitions}}$, the minimum α -value that ensures good data fit can then be computed as the fraction of expected transitions:

$$\alpha_{\text{minimum}} = \frac{N_{\text{Transitions}}}{N_{\text{TL}}} \quad (12)$$

For α -values smaller than α_{minimum} , the time-lapse model misfit χ_{TL} grows above one and the inversion can be trapped in a minimum with data misfit χ_d above one as well. On the other hand, for α -values bigger than α_{minimum} the model regularization plays a smaller role in the objective function and the resulting time-lapse changes may be less compact. This also means that selecting α before inversion imposes a maximum to the number of transitions allowed to occur by the minimum support functional, that is, α represents the maximum relative variation (for values below 1). When it is difficult to predict the number of expected transitions $N_{\text{Transitions}}$ of a time-lapse experiment from the prior information, the classic L2 inversion can be used for estimating $N_{\text{Transitions}}$ and consequently α_{minimum} , as it will be shown in the field example.

3.2 Synthetic tests and interpretation

In order to test the generalized minimum support functional expressed in (eqs 10a and 10b), we decided to use a set of simple synthetic models, mimicking the process of a growing conductive plume. The models are composed by conductive anomalies with a resistivity ratio of 0.75 with respect to the surrounding background (that has a homogeneous resistivity equal to 400 Ωm). As reference model $\mathbf{m}_{\text{reference}}$ in eq. (2) we decided to use the homogeneous background itself. This choice is different from that of, for example, Rosas Carbajal *et al.* (2012), where the inversion of a more complex background model was used as reference model. We opted for this approach in order to simplify the interpretation: choosing a homogeneous reference model, the differences in the time-lapse inversions are only due to the different regularizations, and are not influenced by the way in which the lack of knowledge of the background affects the time-lapse results. All the synthetic data used in the time-lapse inversions presented in the following were generated using the same multiple gradient sequence (Dahlin & Zhou 2004) as adopted in the field example (Doetsch *et al.* 2015a), composed by 910 quadrupoles on 64 electrodes at 2 m spacing. Uncorrelated Gaussian noise with standard deviation equal to 2 per cent of the data values was added to the synthetic data.

Fig. 2 presents the comparison of the L2 norm and the generalized minimum support norm on one of these synthetic examples, representative of the results obtained with all the other synthetic models that are shown in the following. The plots show the ratio of the time-lapse inversion results and the reference model. Thus

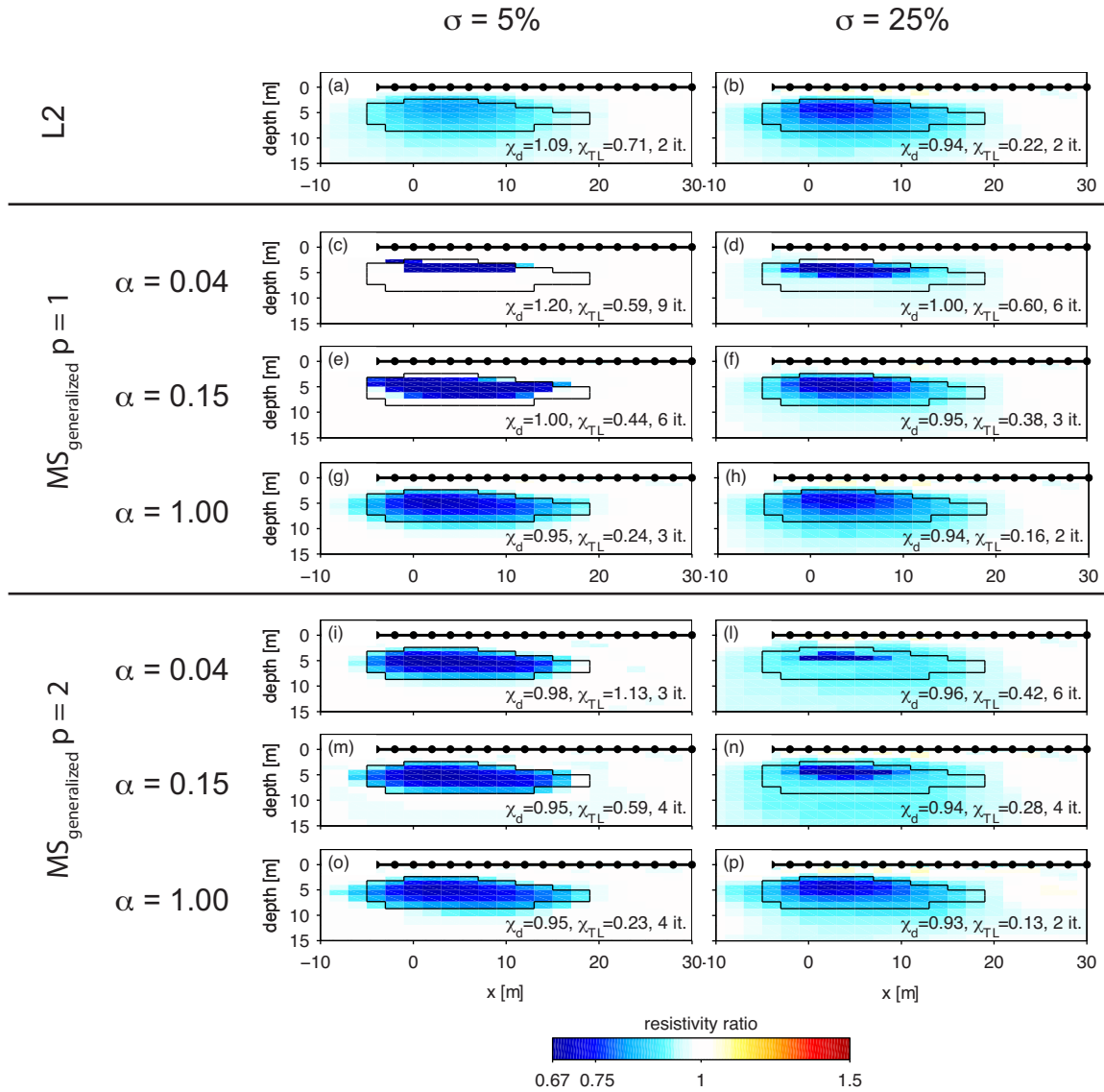


Figure 2. Comparison of inversion results when using different norms and norm settings. The synthetic data were created using an input model with a resistivity ratio of 0.75 within the outlined plume (black line) and 1 outside, and adding 2 per cent Gaussian noise. The left and right columns show inversions with an *a-priori* σ of 5 per cent and 25 per cent, respectively. Panels a and b correspond to L2 norm; panels c–h correspond to $p = 1$ generalized minimum support; panels i–p correspond to $p = 2$ generalized minimum support (i.e. to sharper norm transition around the threshold σ). See eq. (10b) and the text for a description of α , σ and p .

values below 1 indicate a decrease and values above 1 indicate an increase in resistivity compared to the reference model.

The results are displayed for different values of the three tuning settings (i.e. the threshold σ , the maximum relative variation α and the transition sharpness p):

- (1) Two σ -values, 5 per cent and 25 per cent, equal to one fifth of the synthetic resistivity ratio and to the resistivity ratio itself, respectively.
- (2) Two p -values, that is, 1 and 2. With these values the $MS_{\text{generalized}}$ measure needs two and one decade around the threshold σ to reach 99 per cent of the transition, respectively.
- (3) Three α -values, i.e. 0.04, 0.15 and 1.0. The 0.04 value is the α_{minimum} value defined by eq. (12) for the synthetic plume. On the contrary, the $\alpha = 1.0$ value gives a time-lapse misfit $\chi_{TL} = 1$ only if all the model parameters variations are above the threshold σ .

In Fig. 2 there is a clear difference between the L2 and the $MS_{\text{generalized}}$ results, and also the effects of σ , p and α are evident. The L2 inversions (Figs 2a and b) are affected by the change in σ , because in the L2 implementation used in this study the time-lapse model variation are weighted through C_{TL}^{-1} , but neither α nor p enter the measure. The $\sigma = 5$ per cent L2 inversion is slightly overconstrained, with data misfit above one and a flattened conductive plume. On the contrary, in the $\sigma = 25$ per cent L2 inversion the data are well fitted and the conductive plume is more pronounced, but still significantly smooth, as an effect of the L2 constraints.

The $MS_{\text{generalized}}$ inversions with $p = 1$ (Figs 2c–h) are affected by changes in both σ and α . In particular:

- (1) The $\sigma = 5$ per cent inversions (panels c, e, g) show compact time-lapse changes, while the $\sigma = 25$ per cent time-lapse changes (panels d, f, h) are significantly smoother (L2-like for $\alpha = 1.0$ and $\sigma = 25$ per cent).

(2) The size of the conductive plume increases with α , with both σ -values.

(3) The inversion with $\alpha = 0.04$ and $\sigma = 5$ per cent (panel c) is overconstrained, with data misfit $\chi_{\text{obs}} = 1.2$. Values of α below 0.04 with $\sigma = 5$ per cent prevent the inversion convergence completely (not shown in the figure for brevity).

The $\text{MS}_{\text{generalized}}$ inversions with $p = 2$ (Figs 2i–p) react differently to the setting changes compared to the $p = 1$ results:

(1) The conductive plumes with $\sigma = 5$ per cent (panels i, m, o) are compact and in very good agreement with the size and resistivity contrast of the synthetic model, with only a very small size increase with α .

(2) The conductive plumes with $\sigma = 25$ per cent (panels l, n, p) are smooth and increase in size with α . But the plumes are more flattened and more dependent on α when compared to the corresponding $p = 1$ results (panels d, f, h).

(3) The difference between the $\sigma = 5$ per cent inversions (panels i, m, o) and the $\sigma = 25$ per cent inversions (panels l, n, p) is more pronounced than with $p = 1$.

(4) Values of α below 0.04 with $\sigma = 5$ per cent prevent the inversion convergence completely (not shown in the figure for brevity).

To summarize, σ defines the sharpness of the time-lapse changes, α controls their size and p regulates the strength of the focusing dependence on both σ and α .

The smaller sensitivity to α of the $p = 2$ results when σ is smaller than the actual variations is a very positive feature, because the plume compactness is driven principally by the data (and not by α). On the other hand, with $p = 2$ the choice of σ is more critical and the plumes are not only smooth, but also somehow flattened when σ is comparable to the model variation. In order to overcome the limits of both the $p = 1$ and $p = 2$ $\text{MS}_{\text{generalized}}$ measures, we developed the asymmetric minimum support functional, presented in the next paragraph.

4 ASYMMETRIC MINIMUM SUPPORT

4.1 Methodology

Is it possible to obtain a minimum support measure that behaves like a $p = 2$ generalized minimum support for low σ , while like a $p = 1$ generalized minimum support for high σ ? In order to answer this question, we have developed a new asymmetric minimum support functional that performs differently above or below the threshold σ . In particular, two sharpness settings, namely p_1 and p_2 , are defined: the asymmetric functional behaves like a $p = p_1$ $\text{MS}_{\text{generalized}}$ measure below σ , while it behaves like a $p = p_2$ functional above σ . The analytical expression of the functional is expressed as a weighted average of the $p = p_1$ and the $p = p_2$ $\text{MS}_{\text{generalized}}$ measures, through the weighting function β :

$$\varphi_{\text{MS}_{\text{asymmetric}}} = \alpha^{-1} \left[(1 - \beta) \cdot \frac{(x_i^2/\sigma_i^2)^{p_1}}{(x_i^2/\sigma_i^2)^{p_1} + 1} + \beta \cdot \frac{(x_i^2/\sigma_i^2)^{p_2}}{(x_i^2/\sigma_i^2)^{p_2} + 1} \right]. \quad (13a)$$

$$\beta = \frac{(x_i^2/\sigma_i^2)^{\max(p_1, p_2)}}{(x_i^2/\sigma_i^2)^{\max(p_1, p_2)} + 1} \quad (13b)$$

Our first test was performed on a functional with $p_1 = 1$ and $p_2 = 2$. The inversion results on synthetic models (similar to the

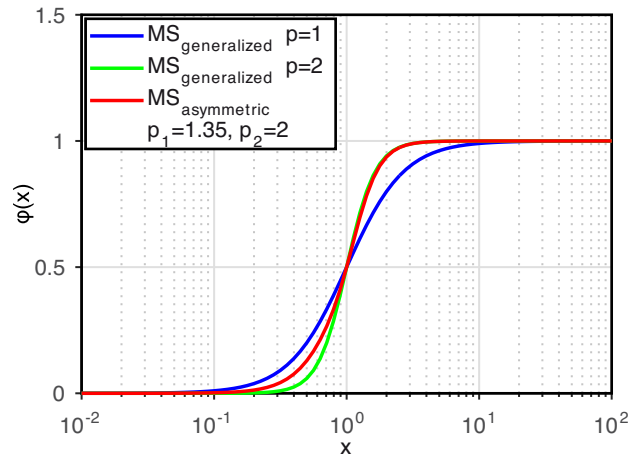


Figure 3. Comparison of generalized minimum support (eqs 10a and 10b) and asymmetric minimum support (eqs 13a and 13b).

one presented in Fig. 2) showed more homogeneous conductive plumes when compared to the $p = 1$ $\text{MS}_{\text{generalized}}$ inversions, but the dependence on α for small σ was almost identical. A significantly better performance was obtained when using $p_1 = 1.35$ and $p_2 = 2$, and these are the sharpness settings that are used in all the following synthetic and field examples. This functional is shown in Fig. 3: it performs in between the $p = 1$ and $p = 2$ generalized measures below σ , while it coincides with the $p = 2$ generalized measure above σ .

4.2 Synthetic tests and interpretation

Fig. 4 presents the $\text{MS}_{\text{asymmetric}}$ results for the synthetic model of Fig. 2. In comparison with the $p = 1$ $\text{MS}_{\text{generalized}}$ inversions, a weaker dependence on α is shown for low σ ; a weaker dependence on σ is also observed when comparing with the $p = 2$ functional. On the contrary, the $p = 1.35$ $\text{MS}_{\text{generalized}}$ inversions show a dependence on σ and α similar to the $p = 1$ $\text{MS}_{\text{generalized}}$ inversions (results not shown in the figure for brevity).

A more quantitative comparison of the results is presented in Fig. 5 by showing a vertical profile through the models of Figs 2 and 4 at $x = 2$ m. Furthermore, the average resistivity ratio in the area comprised between the bottom boundary of the synthetic plume and a depth of 20 m (i.e. the maximum depth shown in Fig. 5) is presented in Table 1 for the $\sigma = 25$ per cent inversion results. Comparing the panels b, d, f and h of Fig. 5 (i.e. the $\sigma = 25$ per cent results) it is notable how the $p = 2$ $\text{MS}_{\text{generalized}}$ inversions flatten the plume and do not tend to 1 at depth, also for $\alpha = 1$. This is also more evident when looking at Table 1, where values of 1 correspond to perfect recovery: the average resistivity ratios are smaller for the $p = 2$ $\text{MS}_{\text{generalized}}$ inversions, meaning that the inversion models are farther from the reference model below the plume. Panels a, c and e of Fig. 5 highlight also the stronger dependence on α of the $p = 1$ $\text{MS}_{\text{generalized}}$, followed by the asymmetric functional and the $p = 2$ one. The results with both small and high σ -values also suggest that an α -value bigger than α_{minimum} (i.e. 0.04 for this synthetic example) represents a more robust choice than α_{minimum} itself, especially for the $p = 1$ generalized minimum support. In fact, with $\chi_{\text{TL}} \rightarrow 1$ the minimum support functionals tend to shrink the time-lapse changes.

Finally, Fig. 6 presents the comparison of the $\text{MS}_{\text{asymmetric}}$ and L2 measures on four different synthetic models, mimicking a

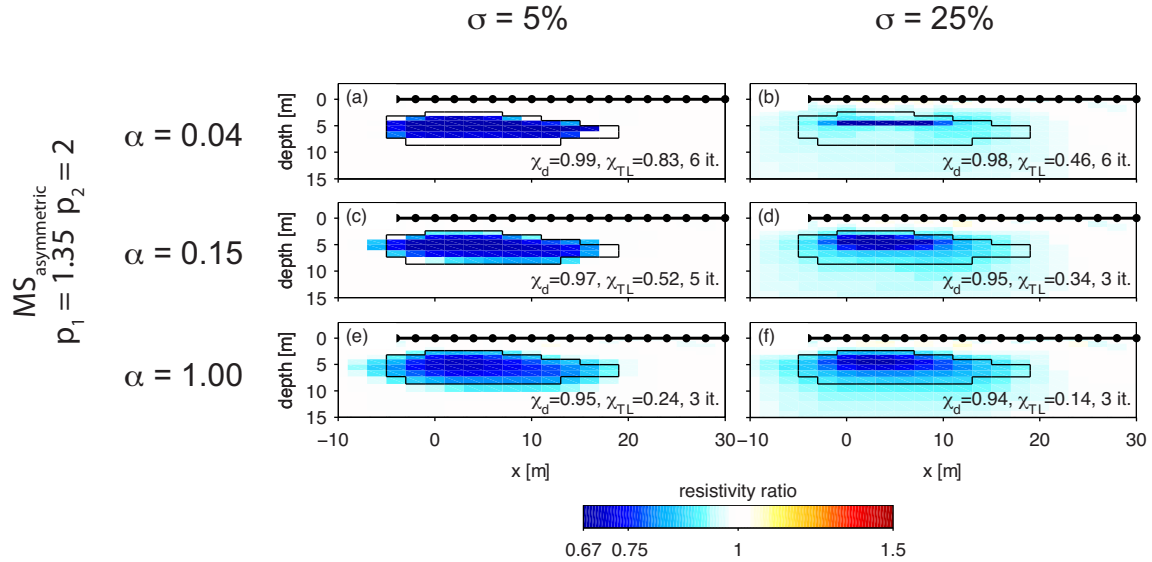


Figure 4. Comparison of asymmetric minimum support inversion results when varying the σ and α norm settings (see eqs 13a and 13b). The synthetic data were created using an input model with a resistivity ratio of 0.75 within the outlined plume (black line) and 1 outside, and adding 2 per cent Gaussian noise. The left and right columns show inversions with an *a-priori* σ of 5 per cent and 25 per cent, respectively.

developing plume. A threshold $\sigma = 5$ per cent and a maximum relative variation $\alpha = 0.15$ were used for all the minimum support inversions, while $\sigma = 25$ per cent was used for the L2 inversions. The $MS_{\text{asymmetric}}$ norm generates much more compact time-lapse changes when compared to the L2 norm, in very good agreement, both in size and resistivity ratio, with the synthetic models. Table 2 shows the number of transitions $N_{\text{Transitions}} = \alpha \Phi_{MS}(\delta \mathbf{m})$ ‘counted’ by the asymmetric norm compared to the actual transitions present in the synthetic models: the average agreement is within 5 per cent. This result is also another verification of the weak dependence of the $MS_{\text{asymmetric}}$ results on α : in fact, the $\alpha = 0.15$ value used in all the inversions of Fig. 6 ranges from around 3 times to 10 times the α_{minimum} values defined by eq. (11) for the synthetic plumes, but the compactness of the inversion models is practically equivalent. A final consideration can be drawn on the relation between the inversion sharpness and the value of the transition threshold σ in comparison with the magnitude of the parameter variation of the time-lapse changes. When the magnitude of the parameter variation is equal to or smaller than σ , the generalized minimum support norms do not fully penalize the parameter variation in the objective function and the inversion result look smooth. Sharp inversion models require σ -values smaller than the magnitude of the parameter variation, but how much smaller?

When the transition threshold σ is smaller than one tenth of a parameter variation δm (i.e. when $\sigma \leq \frac{\delta m}{10}$), the $p = 1$ generalized minimum support reaches 99 per cent of the maximum penalization (i.e. $\varphi_{MS_{\text{generalized}}}(\delta m) \geq 0.99\alpha$). With $p = 2$, half a decade is enough for reaching the maximum penalization, that is, $\sigma \leq \frac{\delta m}{\sqrt{10}}$ implies $\varphi_{MS_{\text{generalized}}}(\delta m) \geq 0.99\alpha$ (see Fig. 1, comparison of blue and green lines). This means that σ smaller than 10 per cent of the magnitude of the parameter variation ensures the full focusing of the $p = 1$ $MS_{\text{generalized}}$ inversions, while σ smaller than ~ 30 per cent of the magnitude of the parameter variation ensures the full focusing of the $p = 2$ $MS_{\text{generalized}}$ and the $p_1 = 1.35$, $p_2 = 2$ $MS_{\text{asymmetric}}$ inversions. Too small values for σ should be avoided as well in the norm tuning, because they penalize insignificant model

variations (from the monitoring point of view) and may produce overconstrained inversion models.

5 OKSBØL FIELD EXAMPLE (DC & IP)

The field example selected for comparing the $MS_{\text{asymmetric}}$ and the L2 norms represents one time-lapse recording of a CO_2 injection monitoring experiment, carried out for investigating the detectability of geochemical changes induced by CO_2 through surface DC and IP measurements. The experiment was performed at Vrøgum plantation near Esbjerg (western Denmark), and comprised both 3-D DC-IP geophysical monitoring (Auken *et al.* 2014b; Doetsch *et al.* 2015a) and an extensive groundwater sampling campaign (Cahill *et al.* 2014).

CO_2 was injected in two screened intervals at 4–5 and 9–10 m depth in two wells separated horizontally by 2 m and arranged to create a curtain of CO_2 perpendicular to the groundwater flow direction (Cahill *et al.* 2014). Injection was started on 2012 May 14, and lasted until July 24, with the total amount of injected CO_2 adding up to 1600 kg in 72 days.

Five parallel profiles with 64 electrodes at 2 m spacing were installed with a cross-line spacing of 5 or 8 m parallel to the groundwater flow (see Auken *et al.* 2014b for more details about the installed system). Here, we concentrate on the central 2-D profile, running through the injection point. This central profile runs in the groundwater flow direction, and results of the 3-D DC inversions as well as the water samples (Auken *et al.* 2014b) show that the main CO_2 pulse follows the direction of this profile.

All DC and full-decay IP data were inverted following Fiandaca *et al.* (2013), where the DC-IP models are parametrized using the Cole–Cole model (Cole & Cole 1941; Pelton *et al.* 1978), defined by the DC resistivity ρ , the chargeability M_0 , the time constant τ and frequency exponent C . In the time-lapse inversion the difference correction (LaBrecque & Yang 2001) was applied to the DC data.

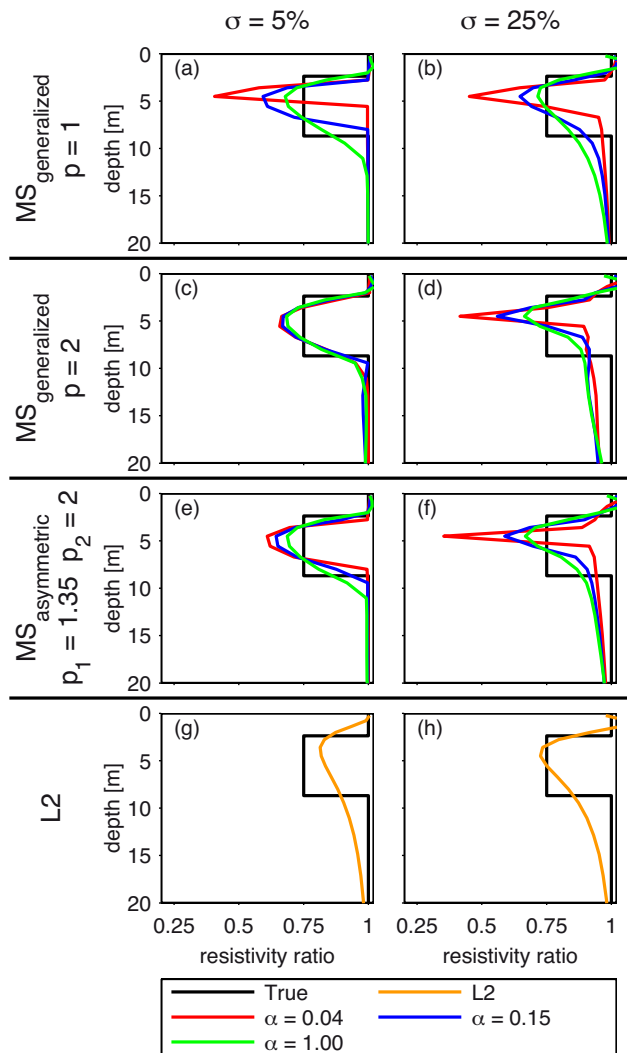


Figure 5. Vertical profile through the models in Figs 2 and 4 at $x = 2$ m. The left and right columns show inversions with an *a-priori* σ of 5 per cent and 25 per cent, respectively. Panels a and b: L2 norm; panels c and d: generalized minimum support norm, $p = 1$; panels e and f: generalized minimum support norm, $p = 2$; panels g and h: asymmetric minimum support norm, $p_1 = 1.35$, $p_2 = 2.0$.

Table 1. Average resistivity ratio in the model area below the synthetic plume for the inversions of Fig. 2 (d), (f), (h) ($p = 1$ column), Fig. 2 (l), (n), (p) ($p = 2$ column) and Fig. 4 (b), (d), (f) ($p_1 = 1.35$, $p_2 = 2$ column).

	$p = 1$	$p = 2$	$p_1 = 1.35, p_2 = 2$
$\sigma = 25$ per cent $\alpha = 0.04$	0.98	0.94	0.97
$\sigma = 25$ per cent $\alpha = 0.15$	0.97	0.93	0.95
$\sigma = 25$ per cent $\alpha = 1.0$	0.95	0.93	0.95

The pre-injection reference inversion is shown in Fig. 7. The resistivity model in Fig. 7(a) confirms the general geology at the site. The unsaturated aeolian sand above 13 m elevation (2 m depth at the centre of the profile) is characterized by high resistivities above 600 Ω m. A layer of intermediate resistivities that characterize the saturated aquifer with aeolian and glacial sands follows the high-resistivity layer. The lowest resistivities (<200 Ω m) are found in the marine sands below 5 m elevation. Generally, the chargeability M_0 section in Fig. 7b shows small values below 100 mV/V, as ex-

pected in this sandy geology. Close to the surface however, there is a thin layer with m_0 around 100 mV/V, which is most likely related to the topsoil. Within the saturated aquifer region, there is some variability in M_0 that is most likely related to silt lenses within the glacial sands. These heterogeneities were also found when drilling the observation wells. The τ section (Fig. 7c) shows intermediate decay times of ~ 0.8 s in the saturated glacial sands and shorter decay times in the shallow aeolian sands, that has smaller grain sizes (Cahill *et al.* 2014). The frequency exponent C shows some variation within the saturated aquifer, with lower values (corresponding to broader frequency spectrum) located in the shallow part.

Fig. 8 presents the time-lapse inversions at day 53 after the injection start, with the $p_1 = 1.35$ and $p_2 = 2$ MS_{asymmetric} norm and the L2 norm. The α and σ settings of the MS_{asymmetric} norm were selected using the complementary information retrieved from the groundwater sampling campaign and using the results of the L2 inversion as well. The order of magnitude of the parameter variation was estimated from the measurements of the electrical conductivity (EC) carried out in the monitoring wells (the measurement points are indicated by the white, black-edged circles in Fig. 8). The EC on average increases of 24 per cent between day 0 and day 53, and a corresponding decrease in the formation resistivity is expected, due to the sandy geology. In order to fully penalize this kind of variation in the objective function, a $\sigma = 5$ per cent transition threshold, equal to around 1/5 of the estimated parameter variation, was selected. The same 5 per cent value was used for all the Cole–Cole parameters, because a similar range of parameter variations is present in the classic L2 inversion for all parameters (except for τ , which shows almost no time-lapse changes). The L2 inversion was carried out with $\sigma = 10$ per cent, because this value gave a better inversion results in comparison with the groundwater monitoring. The area of the L2 time-lapse changes greater than 10 per cent covers 6.9 per cent of the total inversion cells, so $\alpha = 0.3$ was chosen in the MS_{asymmetric} inversion (around four times 0.069, i.e. four times the estimated α_{minimum}). In theory different α -values could be chosen for the four different inversion parameters, for instance for forcing no variations in the τ section in analogy to the L2 inversion, but we keep the same $\alpha = 0.3$ value for all of them for simplicity.

Fig. 8 shows the ratio of the time-lapse inversion result (day 53) and the reference model (day 0). Values below 1 thus indicate a decrease and values above 1 indicate an increase in the respective parameters compared to the pre-injection situation. For comparison, isolines of the EC variations computed from the groundwater sampling are shown on top of the geophysical sections. Considering that EC increases with time, the isolines have been computed on the $\frac{EC_{\text{day0}}}{EC_{\text{day53}}}$ ratio, in order to use the same color scale of the geophysical parameter variations.

Resistivity ρ , chargeability M_0 and frequency exponent C show a clear decrease in their values at the injection wells and, especially resistivity, a little downstream (toward higher x) of the injection. The resistivity section also shows a strong increase in resistivity at shallow depths. This increase in resistivity is due to a decrease in the water table and moisture content of the unsaturated zone. The M_0 and C sections are also affected by the near-surface changes in the unsaturated zone. In comparison, the τ section shows little variation.

The two norms give qualitatively comparable results with equivalent data fit ($\chi_d = 0.79$ and $\chi_d = 0.76$ for the focused and L2 inversions, respectively), with the MS_{asymmetric} inversions showing more compact time-lapse changes, for all the inverted parameters.

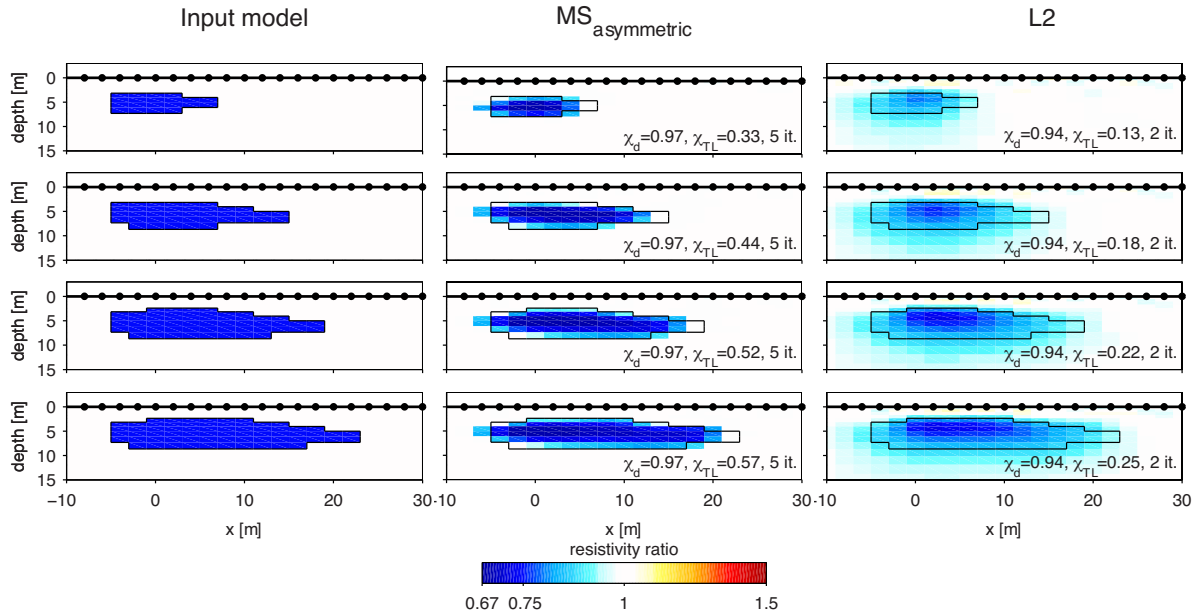


Figure 6. Asymmetric minimum support (middle) and L2 (right) inversion results for different plumes, with all plumes (left) being characterized by a resistivity ratio of 0.75. The focusing inversion uses $\alpha = 0.15$ and $\sigma = 5$ per cent (as in Fig. 2c), while the L2 inversion uses $\sigma = 25$ per cent (as in Fig. 2b). All inversion results fit the data to the error level, with the focused inversion recovering a sharper image of the plumes.

Table 2. Transitions counted by the asymmetric minimum support norm on the inversions of Fig. 6.

	Transitions counted by the asymmetric minimum support norm	True transitions in the synthetic models
Plume 1	22.5	20
Plume 2	40.1	39
Plume 3	56.0	54
Plume 4	67.3	66

In particular, the resistivity model (Fig. 8a) shows a clearer conductive plume extending about 15 m from the injection points, with a good accordance of the lateral extent and the magnitude of the increase in conductivity measured in the same period in the monitoring wells. On the contrary, the L2 resistivity model (Fig. 8b) presents more smeared conductive changes, and it is not possible to infer the lateral extent of the conductive plume correctly. Both inversions underestimate the plume thickness and present shallower time-lapse changes, probably because of a lack of vertical resolution. Also the shallow resistive changes are more compact in the $MS_{\text{asymmetric}}$ inversion, as well as the shallow positive anomalies in M_0 and C .

6 DISCUSSION

The synthetic and field results presented in the previous sections show that compact time-lapse changes can be obtained when using the $MS_{\text{generalized}}$ (eqs 10a and 10b) and $MS_{\text{asymmetric}}$ (eqs 13a and 13b) norms, and that it is possible to give an intuitive meaning to the norm settings. With our approach it is easy to find globally optimal values for all the norm settings, which work well not only on simple synthetic cases, but also on complex field cases, where the size of both the data space and the model space is significantly increased.

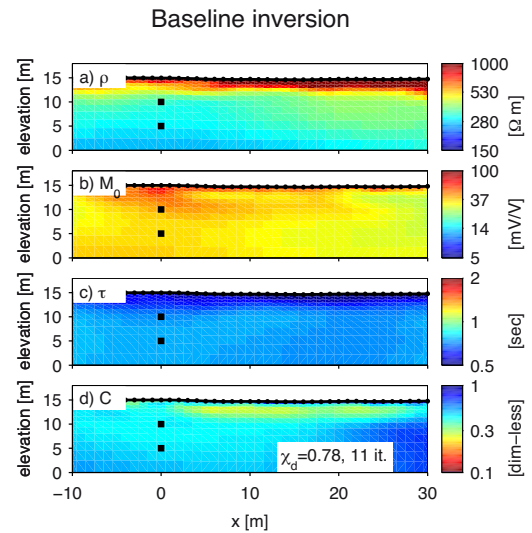


Figure 7. Baseline full-decay DC-IP inversion for the CO₂ injection experiment at Oksbøl, Denmark. CO₂ was injected in two screened intervals at 4–5 and 9–10 m depth, represented by the black squares. Modified after Doetsch *et al.* (2015a).

To summarize, the three norm settings (i.e. σ , α and p) for optimizing the $MS_{\text{generalized}}$ and $MS_{\text{asymmetric}}$ norms can be robustly chosen in the following way:

- (1) The threshold σ should be chosen as a fraction (10–30 per cent) of the expected parameter (e.g. resistivity) variation relative to the baseline model. The 10–30 per cent fraction is needed in order to fully penalize the expected model variations in the objective function, as explained more in detail at the end of the asymmetric minimum support section. The expected model variation can be estimated from the knowledge of the process underlying the time-lapse changes, or can be inferred from a more standard (e.g.

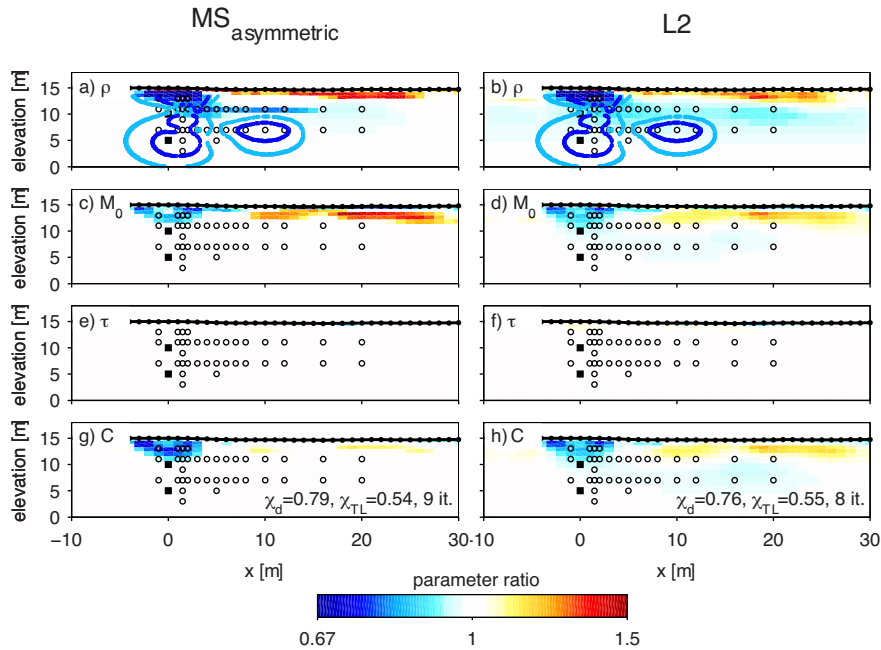


Figure 8. Asymmetric minimum support and L2 full-decay DC-IP time-lapse inversions for the CO₂ injection experiment at day 53 after the beginning of the CO₂ injection. CO₂ was injected in two screened intervals at 4–5 and 9–10 m depth, represented by the black squares. The white circles with black edges show the points where the electrical conductivity (EC) of the water was measured. The blue and light-blue lines of panels (a) and (b) represent the isolines of EC variations at values of 0.75 and 0.85, respectively (in the same color scale of the parameter ratio, but considering $EC_{\text{day } 0}/EC_{\text{day } 53}$ because EC increased over time).

L2) geophysical inversion. In the field example we used an average value for the estimation of the expected variation, but other approaches can be chosen. For instance, the minimum expected variation can be used for determining σ , for obtaining sharp changes also for small time-lapse variations. With this kind of choices for σ , compact time-lapse changes are retrieved, while smooth changes occur with σ equal to or bigger than the expected change itself. Too small σ -values should be avoided in the norm tuning, because they penalize also insignificant (from the monitoring point of view) model variations and may produce overconstrained inversion models.

(2) The maximum relative variation α should be chosen as a function of the expected area/volume fraction α_{minimum} (eq. 12), where time-lapse changes are expected. Again, α_{minimum} can be estimated from the prior knowledge of the monitored geochemical process or from more standard inversion results. α -values bigger than α_{minimum} (3–10 times for the examples of Fig. 6) represent a more robust choice than α_{minimum} itself, because values close to α_{minimum} tend to shrink the time-lapse changes (especially with $p = 1$). On the contrary, too big α -values produce bigger (and smoother) time-lapse changes.

(3) The transition sharpness p controls the dependence of the compactness of the minimum support time-lapse changes on the other two settings σ and α . In particular, the dependence on α decreases when increasing p , while the dependence on σ increases with p . Consequently, low p -values (i.e. $p = 1$) are preferred if a good estimate for α_{minimum} is possible but the expected parameter variation is difficult to infer. On the contrary, high p -values (i.e. $p = 2$) perform better if a good guess for the expected parameter variation is possible. The $MS_{\text{asymmetric}}$ norm (eqs 13a and 13b) with $p_1 = 1.35$ and $p_2 = 2$ represent the best compromise that we found in terms of weak dependence on both σ and α .

All these considerations are illustrated in Fig. 9. A final consideration can be drawn when looking at all the different inversion models with equivalent data misfit obtainable when changing the regularization in the synthetic and field examples presented in this study: the role of the regularization should never be forgotten when interpreting geophysical inversions.

7 CONCLUSIONS

New, generalized expressions for the minimum support norm have been developed. The generalized minimum support norms can be tuned with three settings: (i) the threshold defining the ‘transition’ between changed and non-changed parameters; (ii) the maximum relative variation area; (iii) the sharpness of the transition, definable asymmetrically before and after the transition threshold. Tests on synthetic DC modeling and field DC-IP examples show that the new functionals react in an intuitive and predictable way to these three settings and give reliable and robust results. In particular, the asymmetric generalized minimum support norm represents the best compromise among all the presented measures for time-lapse inversions. The main advantage of the asymmetric norm is its weak dependence on the tuning settings, that is, the transition threshold and the maximum relative variation. In fact, the weak dependence implies that the results are more data-driven and, ultimately, more robust.

In many time-lapse experiments diffusive processes are monitored, and compact time-lapse changes do not necessarily represent the underlying physics/geochemistry. Robust and easy-to-tune regularizations that favour the smallest model variation compatible with the data can be a very helpful tool for data interpretation, when used together with model measures that promote smooth variations.

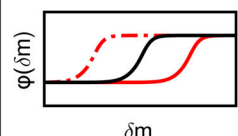
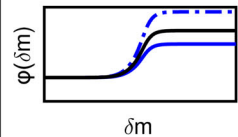
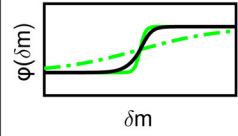
SETTING	MEANING/ EFFECT	OPTIMAL VALUE	VALUE HIGHER THAN OPTIMAL	VALUE LOWER THAN OPTIMAL
 <p style="text-align: center;">δm</p> <p style="text-align: center; color: red; font-size: 2em;">σ</p>	<p>σ represents the transition point of the minimum support functional φ and controls the sharpness of time-lapse changes</p>	<p>σ should be a fraction (10–30%) of the expected parameter variation relative to the reference model</p>	<p>σ values > optimal produce smooth time-lapse changes</p>	<p>σ values < optimal may produce over-constrained inversions</p>
 <p style="text-align: center;">δm</p> <p style="text-align: center; color: blue; font-size: 2em;">α</p>	<p>α controls the relative weight of data and model measures in the objective function and affects the size of time-lapse changes</p>	<p>α should be bigger (3–10 times) than the expected relative area/volume of time-lapse changes (equation (12))</p>	<p>α values > optimal produce bigger time-lapse changes</p>	<p>α values < optimal shrink time-lapse changes</p>
 <p style="text-align: center;">δm</p> <p style="text-align: center; color: green; font-size: 2em;">p</p>	<p>p controls the transition sharpness of φ and determines the way in which the focusing depends on σ and α</p>	<p>asymmetric values ($p_1=1.35$ and $p_2=2$) give the weaker dependence of the focusing on σ and α</p>	<p>the focusing depends more on σ when p values > optimal</p>	<p>the focusing depends more on α when p values < optimal</p>

Figure 9. Tuning the settings of the symmetric and asymmetric generalized minimum support functionals: recap of settings meaning/effect, optimal values and overestimation/underestimation of the setting values. The plots represent the generalized minimum support functional φ of eqs (10) and (13) as a function of the distance δm between a generic parameter and its reference value. Red, blue and green lines represent a modification in the settings σ , α and p , respectively.

ACKNOWLEDGEMENTS

Funding for the work was provided by Formas—The Swedish Research Council for Environment, Agricultural Sciences and Spatial Planning (ref. 2012-1931), BeFo—Swedish Rock Engineering Research Foundation, (ref. 331) and SBUF—The Development Fund of the Swedish Construction Industry (ref. 12719), within the Geoinfra-TRUST framework. This study was also supported by the CO2-GS project (<http://co2gs.geus.net/>) and the HyGEM project (Integrating geophysics, geology, and hydrology for improved groundwater and environmental management, Project no. 11-116763), both funded by the Danish Strategic Research Council.

REFERENCES

- Ajo-Franklin, J., Minsley, B. & Daley, T., 2007. Applying compactness constraints to differential traveltome tomography, *Geophysics*, **72**, R67–R75.
- Archie, G.E., 1942. The electrical resistivity log as an aid in determining some reservoir characteristics, *Trans. AIME*, **146**, 54–62.
- Auken, E. *et al.*, 2014a. An overview of a highly versatile forward and stable inverse algorithm for airborne, ground-based and borehole electromagnetic and electric data, *Explor. Geophys.*, **46**(3), 223–235.
- Auken, E., Doetsch, J., Fiandaca, G., Christiansen, A.V., Gazoty, A., Cahill, A.G. & Jakobsen, R., 2014b. Imaging subsurface migration of dissolved CO₂ in a shallow aquifer using 3-D time-lapse electrical resistivity tomography, *J. appl. Geophys.*, **101**, 31–41.
- Binley, A., Winship, P., West, L.J., Pokar, M. & Middleton, R., 2002. Seasonal variation of moisture content in unsaturated sandstone inferred from borehole radar and resistivity profiles, *J. Hydrol.*, **267**, 160–172.
- Blaschek, R., Hördt, A. & Kemna, A., 2008. A new sensitivity-controlled focusing regularization scheme for the inversion of induced polarization data based on the minimum gradient support, *Geophysics*, **73**(2), F45–F54.
- Brooks, D.H., Ahmad, G.F., MacLeod, R.S. & Maratos, G.M., 1999. Inverse electrocardiography by simultaneous imposition of multiple constraints, *IEEE Trans. Biomed. Eng.*, **46**(1), 3–18.
- Cahill, A.G., Marker, P. & Jakobsen, R., 2014. Hydrogeochemical and mineralogical effects of sustained CO₂ contamination in a shallow sandy aquifer: a field-scale controlled release experiment, *Water Resour. Res.*, **50**, 1735–1755.
- Chambers, J.E., Loke, M.H., Ogilvy, R.D. & Meldrum, P.I., 2004. Non-invasive monitoring of DNAPL migration through a saturated porous medium using electrical impedance tomography, *J. Contaminant Hydrol.*, **68**, 1–22.
- Cole, K.S. & Cole, R.H., 1941. Dispersion and absorption in dielectrics, *J. Chem. Phys.*, **9**, 341–351.
- Coscia, I., Linde, N., Greenhalgh, S., Günther, T. & Green, A.G., 2012. A filtering method to correct time-lapse 3D ERT data and improve imaging of natural aquifer dynamics, *J. appl. Geophys.*, **80**, 12–24.
- Dahlin, T. & Zhou, B., 2004. A numerical comparison of 2D resistivity imaging with 10 electrode arrays, *Geophys. Prospect.*, **52**, 379–398.
- Daily, W., Ramirez, A., LaBrecque, D. & Nitao, J., 1992. Electrical resistivity tomography of vadose water movement, *Water Resour. Res.*, **28**, 1429–1442.
- Descloitres, M., Ruiz, L., Sekhar, M., Legchenko, A. & Braun, J.J., MohanKumar, M.S. & Subramanian, S., 2008. Characterization of

- seasonal local recharge using electrical resistivity tomography and magnetic resonance sounding, *Hydrol. Process.*, **22**, 384–394.
- Doetsch, J., Fiandaca, G., Auken, E., Christiansen, A.V., Cahill, A.G. & Jacobsen, J.D., 2015a. Field scale time-domain spectral induced polarization monitoring of geochemical changes induced by injected CO₂ in a shallow aquifer, *Geophysics*, **80**, WA113–WA126.
- Doetsch, J., Ingemann-Nielsen, T., Christiansen, A.V., Fiandaca, G., Auken, E. & Elberling, B., 2015b. Direct current (DC) resistivity and induced polarization (IP) monitoring of active layer dynamics at high temporal resolution, *Cold Reg. Sci. Technol.*, **119**, 16–28.
- Doetsch, J., Linde, N., Vogt, T., Binley, A. & Green, A.G., 2012. Imaging and quantifying salt-tracer transport in a riparian groundwater system by means of 3D ERT monitoring, *Geophysics*, **77**, B207–B218.
- Farquharson, C.G. & Oldenburg, D.W., 1998. Non-linear inversion using general measures of data misfit and model structure, *Geophysics*, **134**, 213–227.
- Fiandaca, G., Ramm, J., Binley, A., Gazoty, A., Christiansen, A.V. & Auken, E., 2013. Resolving spectral information from time domain induced polarization data through 2-D inversion, *Geophys. J. Int.*, **192**, 631–646.
- Flores Orozco, A., Williams, K.H., Long, P.E., Hubbard, S.S. & Kemna, A., 2011. Using complex resistivity imaging to infer biogeochemical processes associated with bioremediation of an uranium-contaminated aquifer, *J. geophys. Res.*, G03001, doi:10.1029/2010JG001591.
- French, H. & Binley, A., 2004. Snowmelt infiltration: monitoring temporal and spatial variability using time-lapse electrical resistivity, *J. Hydrol.*, **297**, 174–186.
- Hauck, C., 2002. Frozen ground monitoring using DC resistivity tomography, *Geophys. Res. Lett.*, **29**(21), 2016, doi:10.1029/2002GL014995.
- Hayley, K., Pidlisecky, A. & Bentley, L.R., 2011. Simultaneous time-lapse electrical resistivity inversion, *J. appl. Geophys.*, **75**, 401–411.
- Hermans, T., Nguyen, F., Robert, T. & Revil, A., 2014. Geophysical methods for monitoring temperature changes in shallow low enthalpy geothermal systems, *Energies*, **7**, 5083–5118.
- Hermans, T., Wildemeersch, S., Jamin, P., Orban, P., Brouyère, S., Darsargues, A. & Nguyen, F., 2015. Quantitative temperature monitoring of a heat tracing experiment using cross-borehole ERT, *Geothermics*, **53**, 14–26.
- Johnson, T., Versteeg, R., Ward, A., Day-Lewis, F. & Revil, A., 2010. Improved hydrogeophysical characterization and monitoring through parallel modeling and inversion of time-domain resistivity and induced-polarization data, *Geophysics*, **75**, WA27–WA41.
- Karaoulis, M., Revil, A., Werkema, D.D., Minsley, B.J., Woodruff, W.F. & Kemna, A., 2011a. Time-lapse three-dimensional inversion of complex conductivity data using an active time constrained (ATC) approach, *Geophys. J. Int.*, **187**, 237–251.
- Karaoulis, M.C., Kim, J.H. & Tsourlos, P.I., 2011b. 4D active time constrained resistivity inversion, *J. appl. Geophys.*, **73**, 25–34.
- Kim, J.H., Supper, R., Tsourlos, P. & Yi, M.J., 2013. Four-dimensional inversion of resistivity monitoring data through Lp norm minimizations, *Geophys. J. Int.*, **195**, 1640–1656.
- Kim, J.H., Yi, M.J., Park, S.G. & Kim, J.G., 2009. 4-D inversion of DC resistivity monitoring data acquired over a dynamically changing earth model, *J. appl. Geophys.*, **68**, 522–532.
- Kim, K.J. & Cho, I.K., 2011. Time-lapse inversion of 2D resistivity monitoring data with a spatially varying cross-model constraint, *J. appl. Geophys.*, **74**, 114–122.
- LaBrecque, D. & Yang, X., 2001. Difference inversion of ERT data: a fast inversion method for 3-D *in situ* monitoring, *J. Environ. Eng. Geophys.*, **6**, 83–89.
- Last, B.J. & Kubik, K., 1983. Compact gravity inversion, *Geophysics*, **48**, 713–721.
- Marquart, D., 1963. An algorithm for least squares estimation of nonlinear parameters, *SIAM J. appl. Math.*, **11**, 431–441.
- Menke, W., 1989. *Geophysical Data Analysis: Discrete Inverse Theory*, Academic Press.
- Miller, C., Routh, P., Brosten, T. & McNamara, J., 2008. Application of time-lapse ERT imaging to watershed characterization, *Geophysics*, **73**, G7–G17.
- Minsley, B.J., Sogadem, J. & Morgan, F.D., 2007. Three-dimensional source inversion of self-potential data, *J. geophys. Res.*, **112**, B02202, doi:10.1029/2006JB004262.
- Oldenborger, G.A., Knoll, M.D., Routh, P.S. & LaBrecque, D., 2007. Time-lapse ERT monitoring of an injection/withdrawal experiment in a shallow unconfined aquifer, *Geophysics*, **72**, F177–F187.
- Pelton, W.H., Ward, S.H., Hallof, P.G., Sill, W.R. & Nelson, P.H., 1978. Mineral discrimination and removal of inductive coupling with multifrequency induced-polarization, *Geophysics*, **43**, 588–609.
- Portniaquine, O. & Zhdanov, M.S., 1999. Focusing geophysical inversion images, *Geophysics*, **64**, 874–887.
- Rosas Carbajal, M., Linde, N. & Kalscheuer, T., 2012. Focused time-lapse inversion of radio and audio magnetotelluric data, *J. appl. Geophys.*, **84**, 29–38.
- Singha, K., Day-Lewis, F.D., Johnson, T. & Slater, L.D., 2014. Advances in interpretation of subsurface processes with time-lapse electrical imaging, *Hydrol. Process.*, **29**(6), 1549–1576.
- Slater, L., Binley, A.M., Daily, W. & Johnson, R., 2000. Cross-hole electrical imaging of a controlled saline tracer injection, *J. appl. Geophys.*, **44**, 85–102.
- Vignoli, G., Deiana, R. & Cassiani, G., 2012. Focused inversion of vertical radar profile (VRP) traveltimes data, *Geophysics*, **77**, H9–H18.
- Vignoli, G., Fiandaca, G., Christiansen, A.V., Kirkegaard, C. & Auken, E., 2015. Sharp spatially constrained inversion with applications to transient electromagnetic data, *Geophys. Prospect.*, **63**(1), 243–255.
- Williams, K.H. *et al.*, 2009. Geophysical monitoring of coupled microbial and geochemical processes during stimulated subsurface bioremediation, *Environ. Sci. Technol.*, **43**, 6717–6723.
- Zhdanov, M. & Tolstaya, E., 2004. Minimum support nonlinear parametrization in the solution of a 3D magnetotelluric inverse problem, *Inverse Probl.*, **20**, 937–952.
- Zhdanov, M.S., Vignoli, G. & Ueda, T., 2006. Sharp boundary inversion in crosswell traveltimes tomography, *J. Geophys. Eng.*, **3**, 122–134.